

# Non-exhibition of Bragg phenomenon by chevronic sculptured thin films: experiment and theory

Vikas Vepachedu,<sup>†</sup> Patrick D. McAtee,<sup>†</sup> and Akhlesh Lakhtakia\*

The Pennsylvania State University, Department of Engineering Science and Mechanics,  
NanoMM—Nanoengineered Metamaterials Group, 212 EES Building,  
University Park, PA 16802, USA

\*Corresponding author: akhlesh@psu.edu

<sup>†</sup>These authors contributed equally to this paper.

## Abstract

The unit cell of a chevronic sculptured thin film (ChevSTF) comprises two identical columnar thin films (CTFs) except that the nanocolumns of the first are oriented at an angle  $\chi$  and nanocolumns of the second are oriented at an angle  $\pi - \chi$  with respect to the interface of the two CTFs. A ChevSTF containing 10 unit cells was fabricated using resistive-heating physical vapor deposition of zinc selenide. Planewave reflectance and transmittance spectrums of this ChevSTF were measured for a wide variety of incidence conditions over the 500–900-nm range of the free-space wavelength. Despite its structural periodicity, the ChevSTF did not exhibit the Bragg phenomenon. Theoretical calculations with the CTFs modeled as biaxial dielectric materials indicated that the Bragg phenomenon would not be manifested for normal and near-normal incidence, but vestigial manifestation was possible for sufficiently oblique incidence. Thus, structural periodicity does not always lead to electromagnetic periodicity that underlies the exhibition of the Bragg phenomenon.

Keywords: Bragg mirror, Bragg phenomenon, chevronic sculptured thin films, columnar thin film,

## 1 Introduction

The reflection of X rays of a specific wavelength incident on a crystal from a specific direction is intensely peaked in specific directions that are characteristic of the structural periodicity of the arrangement of atoms in the crystal. A simple relationship describing this phenomenon is attributed to the father-son duo W. H. Bragg and W. L. Bragg [1, 2]. The underlying mathematical treatment deriving from a rigorous application of the frequency-domain Maxwell equations was provided by Ewald [3].

The Bragg phenomenon is exhibited also by a periodically nonhomogeneous material, albeit at optical and lower frequencies [4, 5, 6]. Plane waves incident from any direction in a certain sector of the full solid angle are highly reflected by a half space occupied by a periodically nonhomogeneous material, provided that the free-space wavelength lies in a certain spectral regime, thereby indicating the formation of partial bandgaps. If high reflectance occurs for all directions in a certain spectral regime, a full bandgap is said to be exhibited. Periodically nonhomogeneous materials have been commonly called as photonic crystals for the last three decades.

The optical response characteristics of one-dimensional photonic crystals in the form of periodic multilayers were investigated in the late 19th century [7]. Often called Bragg mirrors or distributed Bragg reflectors nowadays, these structures are fabricated by a variety of thin-film techniques [8, 11, 9, 10]. The number  $N$  of periods must be sufficiently high for the Bragg phenomenon to be exhibited well enough for most applications.

When a Bragg mirror comprises only isotropic dielectric materials, its performance is independent of the polarization state of normally incident light. For obliquely incident light, the center wavelengths of the high-reflectance bands—called Bragg regimes—do not depend on the polarization state of the incident light, but the reflectance does.

When a Bragg mirror comprises anisotropic dielectric materials, then the exhibition of the Bragg phenomenon can be polarization dependent even for normally incident light [8, 12]. The simplest anisotropic dielectric material is uniaxial [13], as exemplified by minerals such as calcite, tourmaline, and rutile [14]. Columnar thin films (CTFs) fabricated using a variety of physical vapor deposition (PVD) techniques [9, 8, 15] are also anisotropic dielectric materials that are used in polarization-discriminatory Bragg mirrors [8, 11].

The unit cell of the simplest Bragg mirror comprises two homogeneous layers of dissimilar materials. The relative permittivity dyadics [13] of the two materials must differ in their eigenvalues and/or eigenvectors. But those differences may not be sufficient for the Bragg phenomenon to be exhibited, as has been exemplified by Slepyan and Maksimenko for the following case [16]. Let a Bragg mirror occupy the region  $0 < z < NP$ , where  $N \gg 1$ ,  $P = 2L$  is the period of the unit cell, and  $L$  is the thickness of each of the two layers in the unit cell. Furthermore, let the relative permittivity dyadics of the materials in the two layers be denoted by

$$\left. \begin{aligned} \underline{\underline{\varepsilon}}_1 &= \underline{\underline{S}}_y(\chi) \cdot \underline{\underline{\varepsilon}}_{ref}^o \cdot \underline{\underline{S}}_y^T(\chi) \\ \underline{\underline{\varepsilon}}_2 &= \underline{\underline{S}}_y(\pi - \chi) \cdot \underline{\underline{\varepsilon}}_{ref}^o \cdot \underline{\underline{S}}_y^T(\pi - \chi) \end{aligned} \right\}, \quad (1)$$

where the dyadic

$$\underline{\underline{\varepsilon}}_{ref}^o = \varepsilon_a (\underline{\underline{I}} - \hat{\mathbf{u}}_x \hat{\mathbf{u}}_x) + \varepsilon_b \hat{\mathbf{u}}_x \hat{\mathbf{u}}_x \quad (2)$$

contains the eigenvalues  $\varepsilon_a$  and  $\varepsilon_b$  common to both  $\underline{\underline{\varepsilon}}_1$  and  $\underline{\underline{\varepsilon}}_2$ ,  $\underline{\underline{I}} = \hat{\mathbf{u}}_x \hat{\mathbf{u}}_x + \hat{\mathbf{u}}_y \hat{\mathbf{u}}_y + \hat{\mathbf{u}}_z \hat{\mathbf{u}}_z$  is the identity dyadic, the dyadic

$$\underline{\underline{S}}_y(\xi) = \hat{\mathbf{u}}_y \hat{\mathbf{u}}_y + (\hat{\mathbf{u}}_x \hat{\mathbf{u}}_x + \hat{\mathbf{u}}_z \hat{\mathbf{u}}_z) \cos \xi + (\hat{\mathbf{u}}_z \hat{\mathbf{u}}_x - \hat{\mathbf{u}}_x \hat{\mathbf{u}}_z) \sin \xi \quad (3)$$

indicates a rotation by an angle  $\xi$  about the  $y$  axis in the  $xz$  plane, and the superscript  $T$  denotes the transpose. Equations (1) and (2) indicate that chosen Bragg mirror comprises two uniaxial dielectric materials that are identical except that the optical axis of the first material is oriented at an angle  $\chi \in [0, \pi/2)$  with respect to the  $+x$  axis and the optical axis of the second material is oriented at an angle  $\pi - \chi$  with respect to the  $+x$  axis. The optical axes of both materials lie wholly in the  $xz$  plane. Provided that the wave vector of the incident light is also wholly confined to the  $xz$  plane, theory shows that no reflection or transmission can occur at the interface of the two materials [16, 17], which implies the absence of the Bragg phenomenon [16].

We decided to experimentally verify that theoretical finding of Slepyan and Maksimenko [16]. For that purpose we fabricated a Bragg mirror made of  $N = 10$  unit cells. As this fabrication was accomplished using thermal evaporation [9, 15], a PVD technique, each layer was a CTF with [8, 12]

$$\underline{\underline{\varepsilon}}_{ref}^o = \varepsilon_b \hat{\mathbf{u}}_x \hat{\mathbf{u}}_x + \varepsilon_c \hat{\mathbf{u}}_y \hat{\mathbf{u}}_y + \varepsilon_a \hat{\mathbf{u}}_z \hat{\mathbf{u}}_z \quad (4)$$

instead of Eq. (2). Thus both layers in the unit cell contained a biaxial dielectric material with  $\varepsilon_a \neq \varepsilon_b \neq \varepsilon_c$ . In each period, the nanocolumns of the first CTF are oriented at an angle  $\chi$  and nanocolumns of the second CTF are oriented at an angle  $\pi - \chi$  with respect to the interface of the two CTFs. As the unit cell thus has a chevronic morphology, the Bragg mirror can be classified as a chevronic sculptured thin film (ChevSTF) [15]. Furthermore, we performed optical characterization experiments with the wave vector of the incident plane wave oriented arbitrarily with respect to the  $xz$  plane. Thus, our experimental study was more general than the theoretical investigation of Slepyan and Maksimenko [16]. We also carried out a theoretical exercise with Eq. (4) in order to qualitatively validate our experimental findings.

The plan of this paper is as follows: Section 2 describes the experimental and theoretical techniques that we adopted to investigate the optical response characteristics of ChevSTFs, whose cell comprises two CTFs described by Eqs. (1) and (4). Section 3 presents our experimentally obtained optical data which are compared qualitatively with the results of our theoretical exercise. Finally, Sec. 4 provides concluding remarks. An  $\exp(-i\omega t)$  time-dependence is implicit, with  $\omega$  as the angular frequency,  $i = \sqrt{-1}$ , and  $t$  as time. The free-space wavenumber, the free-space wavelength, and the intrinsic impedance of free space are denoted by  $k_0 = \omega \sqrt{\varepsilon_0 \mu_0}$ ,  $\lambda_0 = 2\pi/k_0$ , and  $\eta_0 = \sqrt{\mu_0/\varepsilon_0}$ , respectively, with  $\mu_0$  and  $\varepsilon_0$  being the permeability and permittivity of free space.

## 2 Methods

### 2.1 Reflectances and Transmittances

The investigated problem can be theoretically formulated as follows. Suppose the region  $0 < z < NP$  is occupied by a periodic multilayer of infinite transverse extent. The electric and magnetic field phasors of

the plane wave incident on the periodic multilayer from the half space  $z < 0$  are given by [15]

$$\left. \begin{aligned} \mathbf{E}_{\text{inc}}(x, y, z) &= (a_s \hat{\mathbf{s}} + a_p \hat{\mathbf{p}}_+) \exp \{ ik_0 [(x \cos \psi + y \sin \psi) \sin \theta_{\text{inc}} + z \cos \theta_{\text{inc}}] \} \\ \mathbf{H}_{\text{inc}}(x, y, z) &= \eta_0^{-1} (a_s \hat{\mathbf{p}}_+ - a_p \hat{\mathbf{s}}) \exp \{ ik_0 [(x \cos \psi + y \sin \psi) \sin \theta_{\text{inc}} + z \cos \theta_{\text{inc}}] \} \end{aligned} \right\},$$

$$z < 0, \quad (5)$$

where  $\theta_{\text{inc}} \in [0^\circ, 90^\circ)$  is the angle of incidence with respect to the  $z$  axis,  $\psi \in [0^\circ, 360^\circ)$  is the angle of incidence with respect to the  $x$  axis in the  $xy$  plane,  $a_s$  is the amplitude of the  $s$ -polarized component of the plane wave, and  $a_p$  is the amplitude of the  $p$ -polarized component of the plane wave. Here and hereafter, the unit vectors

$$\left. \begin{aligned} \hat{\mathbf{s}} &= -\hat{\mathbf{u}}_x \sin \psi + \hat{\mathbf{u}}_y \cos \psi \\ \hat{\mathbf{p}}_{\pm} &= \mp(\hat{\mathbf{u}}_x \cos \psi + \hat{\mathbf{u}}_y \sin \psi) \cos \theta_{\text{inc}} + \hat{\mathbf{u}}_z \sin \theta_{\text{inc}} \end{aligned} \right\} \quad (6)$$

delineate the orientations of the field phasors.

The electric and magnetic field phasors of the reflected plane wave are given by [15]

$$\left. \begin{aligned} \mathbf{E}_{\text{ref}}(x, y, z) &= (r_s \hat{\mathbf{s}} + r_p \hat{\mathbf{p}}_-) \exp \{ ik_0 [(x \cos \psi + y \sin \psi) \sin \theta_{\text{inc}} - z \cos \theta_{\text{inc}}] \} \\ \mathbf{H}_{\text{ref}}(x, y, z) &= \eta_0^{-1} (r_s \hat{\mathbf{p}}_- - r_p \hat{\mathbf{s}}) \exp \{ ik_0 [(x \cos \psi + y \sin \psi) \sin \theta_{\text{inc}} - z \cos \theta_{\text{inc}}] \} \end{aligned} \right\},$$

$$z < 0, \quad (7)$$

and the electric and magnetic field phasors of the transmitted plane wave by [15]

$$\left. \begin{aligned} \mathbf{E}_{\text{tr}}(x, y, z) &= (t_s \hat{\mathbf{s}} + t_p \hat{\mathbf{p}}_+) \exp \{ ik_0 [(x \cos \psi + y \sin \psi) \sin \theta_{\text{inc}} + (z - NP) \cos \theta_{\text{inc}}] \} \\ \mathbf{H}_{\text{tr}}(x, y, z) &= \eta_0^{-1} (t_s \hat{\mathbf{p}}_+ - t_p \hat{\mathbf{s}}) \exp \{ ik_0 [(x \cos \psi + y \sin \psi) \sin \theta_{\text{inc}} + (z - NP) \cos \theta_{\text{inc}}] \} \end{aligned} \right\},$$

$$z > NP. \quad (8)$$

The reflection amplitudes  $r_s$  and  $r_p$ , as well as the transmission amplitudes  $t_s$  and  $t_p$ , have to be determined in terms of the incidence amplitudes  $a_s$  and  $a_p$  in order to find the reflection and transmission coefficients that appear as the elements of the  $2 \times 2$  matrixes in the following relations:

$$\begin{bmatrix} r_s \\ r_p \end{bmatrix} = \begin{bmatrix} r_{ss} & r_{sp} \\ r_{ps} & r_{pp} \end{bmatrix} \begin{bmatrix} a_s \\ a_p \end{bmatrix}, \quad \begin{bmatrix} t_s \\ t_p \end{bmatrix} = \begin{bmatrix} t_{ss} & t_{sp} \\ t_{ps} & t_{pp} \end{bmatrix} \begin{bmatrix} a_s \\ a_p \end{bmatrix}. \quad (9)$$

Co-polarized coefficients have both subscripts identical, but cross-polarized coefficients do not. The square of the magnitude of a reflection or transmission coefficient is the corresponding reflectance or transmittance; thus,  $R_{\text{sp}} = |r_{\text{sp}}|^2$  is the reflectance corresponding to the reflection coefficient  $r_{\text{sp}}$ , and so on. The principle of conservation of energy mandates the constraints  $R_{\text{ss}} + R_{\text{ps}} + T_{\text{ss}} + T_{\text{ps}} \leq 1$  and  $R_{\text{pp}} + R_{\text{sp}} + T_{\text{pp}} + T_{\text{sp}} \leq 1$ , the inequalities turning to equalities only in the absence of dissipation in the region  $0 < z < NP$ .

## 2.2 Theory

More generally than is needed for a ChevSTF, let us use

$$\left. \begin{aligned} \underline{\underline{\varepsilon}}_1 &= \underline{\underline{S}}_y(\chi_1) \cdot (\varepsilon_{b1} \hat{\mathbf{u}}_x \hat{\mathbf{u}}_x + \varepsilon_{c1} \hat{\mathbf{u}}_y \hat{\mathbf{u}}_y + \varepsilon_{a1} \hat{\mathbf{u}}_z \hat{\mathbf{u}}_z) \cdot \underline{\underline{S}}_y^T(\chi_1) \\ \underline{\underline{\varepsilon}}_2 &= \underline{\underline{S}}_y(\pi - \chi_2) \cdot (\varepsilon_{b2} \hat{\mathbf{u}}_x \hat{\mathbf{u}}_x + \varepsilon_{c2} \hat{\mathbf{u}}_y \hat{\mathbf{u}}_y + \varepsilon_{a2} \hat{\mathbf{u}}_z \hat{\mathbf{u}}_z) \cdot \underline{\underline{S}}_y^T(\pi - \chi_2) \end{aligned} \right\} \quad (10)$$

for a periodic multilayer whose unit cell comprises two different CTFs. Furthermore, let  $L_1$  and  $L_2 = P - L_1$  be the two layer thicknesses.

After defining the phasors

$$\left. \begin{aligned} \mathbf{e}(z) &= \mathbf{E}(x, y, z) \exp [-ik_0 (x \cos \psi + y \sin \psi) \sin \theta_{\text{inc}}] \\ \mathbf{h}(z) &= \mathbf{H}(x, y, z) \exp [-ik_0 (x \cos \psi + y \sin \psi) \sin \theta_{\text{inc}}] \end{aligned} \right\}, \quad (11)$$

we find that wave propagation in the two CTFs is governed by the  $4 \times 4$ -matrix ordinary differential equations [15]

$$\left. \begin{aligned} \frac{d}{dz} [\mathbf{f}(z)] &= i [\hat{\mathbf{P}}(\chi_1; \varepsilon_{a_1}, \varepsilon_{b_1}, \varepsilon_{c_1})] [\mathbf{f}(z)] \\ \frac{d}{dz} [\mathbf{f}(z)] &= i [\hat{\mathbf{P}}(\pi - \chi_2; \varepsilon_{a_2}, \varepsilon_{b_2}, \varepsilon_{c_2})] [\mathbf{f}(z)] \end{aligned} \right\}, \quad (12)$$

where the column 4-vector

$$[\mathbf{f}(z)] = [\hat{\mathbf{u}}_x \cdot \mathbf{e}(z) \quad \hat{\mathbf{u}}_y \cdot \mathbf{e}(z) \quad \hat{\mathbf{u}}_x \cdot \mathbf{h}(z) \quad \hat{\mathbf{u}}_y \cdot \mathbf{h}(z)]^T \quad (13)$$

and the  $4 \times 4$  matrix

$$\begin{aligned} [\mathbf{P}(\xi; \varepsilon_a, \varepsilon_b, \varepsilon_c)] &= \omega \begin{bmatrix} 0 & 0 & 0 & \mu_0 \\ 0 & 0 & -\mu_0 & 0 \\ 0 & -\varepsilon_0 \varepsilon_c & 0 & 0 \\ \varepsilon_0 \frac{\varepsilon_a \varepsilon_b}{\varepsilon_a \cos^2 \xi + \varepsilon_b \sin^2 \xi} & 0 & 0 & 0 \end{bmatrix} \\ &+ k_0 \frac{(\varepsilon_a - \varepsilon_b) \sin \theta_{\text{inc}}}{\varepsilon_a \cos^2 \xi + \varepsilon_b \sin^2 \xi} \sin \xi \cos \xi \begin{bmatrix} \cos \psi & 0 & 0 & 0 \\ \sin \psi & 0 & 0 & 0 \\ 0 & 0 & 0 & 0 \\ 0 & 0 & -\sin \psi & \cos \psi \end{bmatrix} \\ &+ \omega \mu_0 \frac{\sin^2 \theta_{\text{inc}}}{\varepsilon_a \cos^2 \xi + \varepsilon_b \sin^2 \xi} \begin{bmatrix} 0 & 0 & \cos \psi \sin \psi & -\cos^2 \psi \\ 0 & 0 & \sin^2 \psi & -\cos \psi \sin \psi \\ 0 & 0 & 0 & 0 \\ 0 & 0 & 0 & 0 \end{bmatrix} \\ &+ \omega \varepsilon_0 \sin^2 \theta_{\text{inc}} \begin{bmatrix} 0 & 0 & 0 & 0 \\ 0 & 0 & 0 & 0 \\ -\cos \psi \sin \psi & \cos^2 \psi & 0 & 0 \\ -\sin^2 \psi & \cos \psi \sin \psi & 0 & 0 \end{bmatrix}. \quad (14) \end{aligned}$$

Accordingly,

$$[\mathbf{f}(NP)] = [\mathbf{M}] [\mathbf{f}(0)], \quad (15)$$

where the  $4 \times 4$  matrix

$$[\mathbf{M}] = \left( \exp \{i [\mathbf{P}(\pi - \chi_2; \varepsilon_{a_2}, \varepsilon_{b_2}, \varepsilon_{c_2})] L_2\} \exp \{i [\mathbf{P}(\chi_1; \varepsilon_{a_1}, \varepsilon_{b_1}, \varepsilon_{c_1})] L_1\} \right)^N. \quad (16)$$

Continuity requirements on the tangential components of the electric and magnetic fields across the interfaces  $z = 0$  and  $z = NP$  give rise to [15]

$$\begin{bmatrix} t_s \\ t_p \\ 0 \\ 0 \end{bmatrix} = [\mathbf{K}]^{-1} [\mathbf{M}] [\mathbf{K}] \begin{bmatrix} a_s \\ a_p \\ r_s \\ r_p \end{bmatrix}, \quad (17)$$

where the  $4 \times 4$  matrix

$$[\mathbf{K}] = \begin{bmatrix} -\sin \psi & -\cos \psi \cos \theta_{\text{inc}} & -\sin \psi & \cos \psi \cos \theta_{\text{inc}} \\ \cos \psi & -\sin \psi \cos \theta_{\text{inc}} & \cos \psi & \sin \psi \cos \theta_{\text{inc}} \\ -\eta_0^{-1} \cos \psi \cos \theta_{\text{inc}} & \eta_0^{-1} \sin \psi & \eta_0^{-1} \cos \psi \cos \theta_{\text{inc}} & \eta_0^{-1} \sin \psi \\ -\eta_0^{-1} \sin \psi \cos \theta_{\text{inc}} & -\eta_0^{-1} \cos \psi & \eta_0^{-1} \sin \psi \cos \theta_{\text{inc}} & -\eta_0^{-1} \cos \psi \end{bmatrix}. \quad (18)$$

The solution of Eq. (17) provides the four reflection coefficients and the four transmission coefficients defined in Eqs. (9).

When  $\psi = 0^\circ$  and  $0^\circ \leq \theta_{\text{inc}} \lesssim 30^\circ$ , the center wavelength  $\lambda_{0_{sm}}^{\text{Br}}$  of the Bragg regime of order  $m$  is predicted to be [8, 18]

$$\lambda_{0_{sm}}^{\text{Br}} = \frac{2}{m} (L_1 \sqrt{\varepsilon_{c_1}} + L_2 \sqrt{\varepsilon_{c_2}}) \cos \theta_{\text{inc}}, \quad m \in \{1, 2, 3, \dots\}, \quad (19)$$

for  $s$ -polarized incidence. Likewise, the center wavelength  $\lambda_{0_{pm}}^{\text{Br}}$  of the Bragg regime of order  $m$  is predicted to be [8, 18]

$$\lambda_{0_{pm}}^{\text{Br}} = \frac{2}{m} (L_1 \sqrt{\varepsilon_{d_1}} + L_2 \sqrt{\varepsilon_{d_2}}) \cos \theta_{\text{inc}} \quad m \in \{1, 2, 3, \dots\}, \quad (20)$$

for  $p$ -polarized incidence, where

$$\varepsilon_{d_n} = \varepsilon_{a_n} \varepsilon_{b_n} (\varepsilon_{a_n} \cos^2 \chi_n + \varepsilon_{b_n} \sin^2 \chi_n)^{-1}, \quad n \in \{1, 2\}. \quad (21)$$

Equations (19) and (20) are predicated on the assumption that the constitutive scalars  $\varepsilon_{a_n}$ , etc., are frequency independent; otherwise, both equations transform from explicit to implicit equations for the determination of the center wavelengths.

## 2.3 Experimental Methods

### 2.3.1 Fabrication of periodic multilayers comprising CTFs

Each periodic multilayer was fabricated using thermal evaporation [19] implemented inside a low-pressure chamber from Torr International (New Windsor, NY, USA). It contains a quartz crystal monitor (QCM) calibrated to measure the growing thin-film's thickness, a receptacle to hold the material to be evaporated, electrodes to resistively heat the receptacle, and a substrate holder positioned about 15 cm above the receptacle. As the chamber was customized to grow sculptured thin films [15], it contains two stepper motors to control the rotation of the substrate holder about two mutually orthogonal axes.

99.995% pure ZnSe (Alfa Aesar, Ward Hill, MA, USA) was the material of choice due to its high bulk index of refraction and low absorption in the visible spectral regime [20, 21], as well as the ease of evaporation. The manufacturer supplied ZnSe lumps that were crushed into a fine powder. A respirator was worn to avoid the toxic effects of ZnSe on the respiratory system [22]. Approximately 4.2 g of ZnSe powder was packed into a tungsten boat (S22-.005W, R. D. Mathis, Long Beach, CA, USA) that served as the receptacle.

A pre-cleaned glass substrate (48300-0025, VWR, Radnor, PA, USA) was further cleaned in an ethanol bath using an ultrasonicator for 10 min on each side. After removal from the bath, the substrate was immediately dried with pressurized nitrogen gas. A straight line was marked on the substrate to serve as the  $x$  axis. The substrate was secured to the substrate holder using Kapton<sup>TM</sup> tape (S-14532, Uline, Pleasant Prairie, WI, USA), and a shutter was interposed between the receptacle and the substrate holder. By the side of the glass substrate, a silicon wafer was positioned in order to grow a sample for imaging on a scanning electron microscope.

The chamber was pumped down to 1  $\mu$ Torr. The current was then slowly increased to  $\sim 100$  A, and the shutter was rotated to allow a collimated position of the ZnSe vapor to reach the substrate. The deposition rate as read through the QCM was manually maintained equal to  $0.4 \pm 0.02$  nm s<sup>-1</sup>. After the deposition was complete, the shutter was rotated to prevent further deposition, the current was brought back to 0 A, the chamber was allowed to cool down for 60 min, and was then exposed to the atmosphere.

Each periodic multilayer was chosen to contain  $N = 10$  unit cells. This required fabrication to be done in two stages, with 5 unit cells deposited in each stage. By keeping the substrate stationary for 387 s for the deposition of each CTF, the value of  $P$  was targeted to be 310 nm. The substrate was rotated by  $180^\circ$  about a central normal axis passing through it in 0.406 s between the depositions of any two consecutive CTFs. The collimated vapor was directed at an angle  $\chi_{v_1} \in (0^\circ, 90^\circ]$  with respect to the plane of the substrate to deposit the first CTF in each period, the corresponding angle being  $\chi_{v_2} \in (0^\circ, 90^\circ]$  for the second CTF in each period.

Two samples were fabricated:

- Sample A: We chose  $\chi_{v_1} = 20^\circ$  and  $\chi_{v_2} = 70^\circ$ , so that Eqs. (10) would hold in a way that would allow the exhibition of the Bragg phenomenon. In consequence of  $\chi_{v_1} \neq \chi_{v_2}$ , we expected that  $L_1 \neq L_2$  [8]. More general than a ChevSTF, Sample A should be a Bragg mirror.
- Sample B: We chose  $\chi_{v_1} = \chi_{v_2} = 20^\circ$ . The equality of  $\chi_{v_1}$  and  $\chi_{v_2}$  would ensure that Eqs. (1) and (4) hold, and we also expected that  $L_1 = L_2$  ideally. Thus, Sample B should be a ChevSTF.

Our choices of  $\chi_{v_1}$  and  $\chi_{v_2}$  for Samples A and B were guided by the measured relative permittivity dyadics of CTFs of three different materials [8, 23]. The QCM tooling factors were 184 for Samples A and 273 for Sample B.

### 2.3.2 Optical Characterization

Transmittance and reflectance measurements for both Samples A and B were made no more than 24 h after fabrication. Each sample was kept in a desiccator up until the time of characterization in order to prevent degradation due to moisture adsorption.

The experimental setups for reflection and transmission measurements are described in detail elsewhere [24]. Briefly, light from a halogen source (HL-2000, Ocean Optics, Dunedin, FL, USA) was passed through a fiber-optic cable and then through a linear polarizer (GT10, ThorLabs, Newton, NJ, USA); it was either reflected from or transmitted through the sample to be characterized; and was then passed through a second linear polarizer (GT10, ThorLabs) and a fiber-optic cable to a CCD spectrometer (HRS-BD1-025, Mightex Systems, Pleasanton, CA, USA). The transmittances  $T_{ss}$ ,  $T_{ps}$ ,  $T_{pp}$ , and  $T_{sp}$  were measured for  $\theta_{\text{inc}} \in [0^\circ, 70^\circ]$  and  $\psi \in \{0^\circ, 90^\circ\}$ , and the reflectances  $R_{ss}$ ,  $R_{ps}$ ,  $R_{pp}$ , and  $R_{sp}$  for  $\theta_{\text{inc}} \in [10^\circ, 70^\circ]$  and  $\psi \in \{0^\circ, 90^\circ\}$ .

All data were taken in a dark room to avoid noise from external sources. First, the detector measured the intensity  $I_{\text{dark}}$  when the incident light was switched off, no sample was present, and both polarizers had been removed. Then the intensity  $I_s$  or  $I_p$  was measured by the detector with no sample present, the first polarizer set to make the incident light either *s* or *p* polarized, and the second polarizer set to pass light of the same linear polarization state. Then, the sample was inserted, the second polarizer was set to make the detected light either *s* or *p* polarized, and the intensity  $\tilde{I}_s$  or  $\tilde{I}_p$  was recorded. In this way, the measured value of  $T_{sp}$  was

$$T_{sp} = \frac{\tilde{I}_s - I_{\text{dark}}}{I_p - I_{\text{dark}}}, \quad (22)$$

and similarly for the other seven reflectances and transmittances. These measurements were made for  $\lambda_0 \in [500, 900]$  nm.

### 2.3.3 Morphological Characterization

The cross-sectional morphologies of both Samples A and B were characterized using an FEI Nova<sup>TM</sup> NanoSEM 630 (FEI, Hillsboro, OR, USA) field-emission scanning electron microscope. To get a clear image of morphology away from any edge-growth effects, each sample was cleaved using the freeze-fracture technique. This technique is delicate enough to preserve biological samples [25]. All samples were sputtered with iridium using a Quorum Emitech<sup>©</sup> K575X (Quorum Technologies, Ashford, Kent, United Kingdom) sputter coater before imaging.

## 3 Results and Discussion

### 3.1 Morphology

Figure 1 presents a cross-sectional scanning-electron micrograph of Sample A fabricated by setting  $\chi_{v_1} = 20^\circ$  and  $\chi_{v_2} = 70^\circ$ . Eight of the 10 unit cells are clearly evident with  $P \simeq 313$  nm. Whereas the nanocolumns in one of the two CTFs in a unit cell are inclined at  $36.1^\circ$  with respect to the  $+x$  axis, those in the other CTF are inclined at  $102.6^\circ$  with respect to the  $+x$  axis. Thus, the conditions set forth as Eqs. (10) are fulfilled

with  $\chi_1 \simeq 36.1^\circ$  and  $\chi_2 \simeq 77.4^\circ$ . Furthermore,  $L_1 \simeq 0.25P$  whereas  $L_2 \simeq 0.75P$ , because  $\chi_{v_1}$  differs from  $\chi_{v_2}$ . Sample A is clearly not a ChevSTF. Parenthetically, the inequalities  $\chi_1 > \chi_{v_1}$  and  $\chi_2 > \chi_{v_2}$  are in consonance with a plethora of morphological data on CTFs [8, 26].

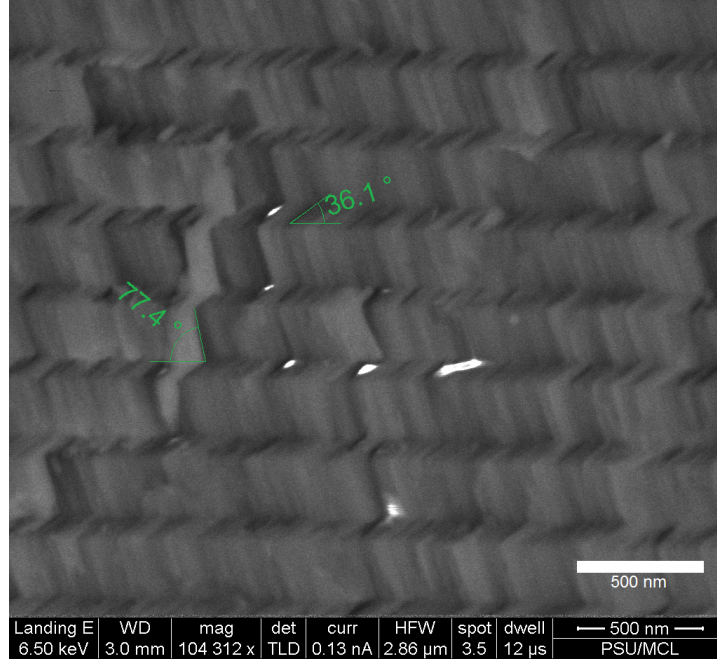


Figure 1: Cross-sectional scanning-electron micrograph of Sample A (fabricated with  $\chi_{v_1} = 20^\circ$  and  $\chi_{v_2} = 70^\circ$ ) on a silicon wafer.

Figure 2 presents a cross-sectional scanning-electron micrograph of Sample B fabricated by setting  $\chi_{v_1} = \chi_{v_2} = 20^\circ$ . All 10 unit cells of this sample are clearly evident with  $P \simeq 308$  nm and  $L_1 \simeq L_2 \simeq P/2$ . Whereas the nanocolumns in one of the two CTFs in a unit cell are inclined at  $37.3^\circ$  with respect to the  $+x$  axis, those in the other CTF are inclined at  $142.8^\circ$  with respect to the  $+x$  axis. Thus, the conditions set forth as Eqs. (1) and (4) are fulfilled with  $\chi \simeq 37.25^\circ$ , and Sample B is a ChevSTF.

### 3.2 Theoretical Results

Experimental data on the relative permittivity dyadics of CTFs fabricated by evaporating ZnSe are unavailable, but the data on the relative permittivity dyadics of CTFs fabricated by evaporation of  $\text{TiO}_2$  are available [23]. The bulk refractive index of ZnSe is 2.5435 at  $\lambda_0 = 700$  nm [27], whereas that of  $\text{TiO}_2$  is 2.5512 at the same wavelength [28]. The closeness of the two bulk refractive indexes allowed us to substitute ZnSe by  $\text{TiO}_2$  for theoretical calculations that can be qualitatively compared with the experimental results.

For  $\chi_{v_1} = 20^\circ$ , data derived from optical-characterization experiments on CTFs of  $\text{TiO}_2$  at  $\lambda_0 = 633$  nm [23] are as follows:  $\chi_1 = 46.367^\circ$ ,  $\varepsilon_{a_1} = 2.5135$ ,  $\varepsilon_{b_1} = 3.9428$ , and  $\varepsilon_{c_1} = 3.1525$ . Likewise, for  $\chi_{v_2} = 70^\circ$ , data derived from the same optical experiments are as follows:  $\chi_2 = 82.802^\circ$ ,  $\varepsilon_{a_2} = 5.5054$ ,  $\varepsilon_{b_2} = 5.8581$ , and  $\varepsilon_{c_2} = 5.5785$ . For a Bragg mirror comprising  $\text{TiO}_2$  CTFs with  $\chi_{v_1} = 20^\circ$ ,  $\chi_{v_2} = 70^\circ$ ,  $L_1 = 77.5$  nm, and  $L_2 = 232.5$  nm (similar to Sample A), Eqs. (19) and (20) yield  $\lambda_{0s_2}^{Br} = 686.74$  nm and  $\lambda_{0p_2}^{Br} = 680.87$  nm when  $\theta_{\text{inc}} = \psi = 0^\circ$ . For a ChevSTF comprising  $\text{TiO}_2$  CTFs with  $\chi_{v_1} = \chi_{v_2} = 20^\circ$  and  $L_1 = L_2 = 155$  nm (similar to Sample B),  $\lambda_{0s_2}^{Br} = 550.41$  nm and  $\lambda_{0p_2}^{Br} = 540.32$  nm when  $\theta_{\text{inc}} = \psi = 0^\circ$ , according to Eqs. (19) and (20).

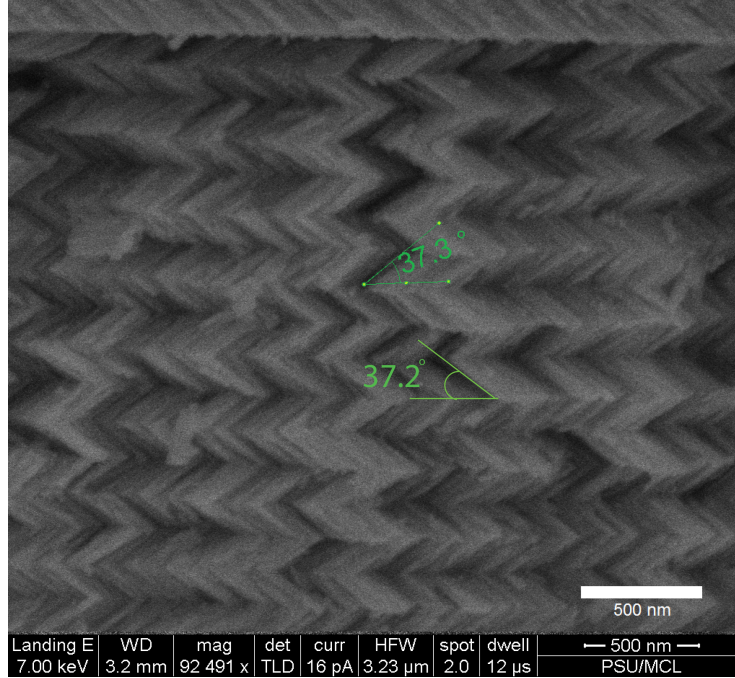


Figure 2: Cross-sectional scanning-electron micrograph of Sample B (fabricated with  $\chi_{v_1} = \chi_{v_2} = 20^\circ$ ) on a silicon wafer.

### 3.2.1 Bragg mirror

In order to present the characteristic features of the Bragg phenomenon, let us begin with the spectrums of all eight remittances calculated for the Bragg mirror comprising  $\text{TiO}_2$  CTFs  $\chi_{v_1} = 20^\circ$ ,  $\chi_{v_2} = 70^\circ$ ,  $L_1 = 77.5$  nm, and  $L_2 = 232.5$  nm (corresponding to Sample A). These remittances are presented as functions of  $\lambda_0 \in [400, 1000]$  nm and  $\theta_{\text{inc}} \in [0^\circ, 90^\circ]$  in Fig. 3 for  $\psi = 0^\circ$  and in Fig. 4 for  $\psi = 90^\circ$ . For all calculations we set  $N = 30$  in order to ensure that the Bragg phenomenon is manifested well [11, 29].

Evidence of the Bragg phenomenon of order  $m \in \{2, 3\}$  is easy to find in Fig. 3. This becomes clear on comparison with the predictions  $\lambda_{0s_2}^{Br} = 686.74$  nm,  $\lambda_{0p_2}^{Br} = 680.87$  nm,  $\lambda_{0s_3}^{Br} = 457.83$  nm, and  $\lambda_{0p_3}^{Br} = 453.91$  nm, of Eqs. (19) and (20) for  $\theta_{\text{inc}} = \psi = 0^\circ$ . The high-reflectance band of order  $m \in \{2, 3\}$  in the plot of  $R_{\text{ss}}$  is slightly redshifted from the high-reflectance band of order  $m \in \{2, 3\}$  in the plot of  $R_{\text{pp}}$ . Furthermore, the Bragg regime of order  $m \in \{2, 3\}$  is blueshifted with increase in  $\theta_{\text{inc}}$ . Both high-reflectance bands are mirrored by low-transmittance bands in the plots of  $T_{\text{ss}}$  and  $T_{\text{pp}}$ .

With  $\lambda_{0s_1}^{Br} = 1373.48$  nm and  $\lambda_{0p_1}^{Br} = 1361.74$  nm predicted by Eqs. (19) and (20), evidence of the Bragg phenomenon of order  $m = 1$  is absent from Fig. 3. This is not surprising because the plots in this figure were drawn for only  $\lambda_0 \in [400, 1000]$  nm. By direct computation, we have verified the existence of high-reflectance bands in the plots of  $R_{\text{ss}}$  and  $R_{\text{pp}}$ , as well as of low-transmittance bands in the plots of  $T_{\text{ss}}$  and  $T_{\text{pp}}$ , that signify the existence of the Bragg phenomenon for  $m = 1$ .

Although no convenient formula is available to predict the center wavelengths for  $\psi \in (0^\circ, 180^\circ)$ , comparison of Figs. 3 and 4 suffices to convince that the latter also provides evidence of the Bragg phenomenon of order  $m \in \{2, 3\}$ . The spectral characteristics of the high-reflectance bands in the plots of  $R_{\text{ss}}$  and  $R_{\text{pp}}$  in Fig. 4 are the same as in Fig. 3. We found similar characteristics for several values of  $\psi \notin \{0^\circ, 90^\circ\}$  (data not presented here).



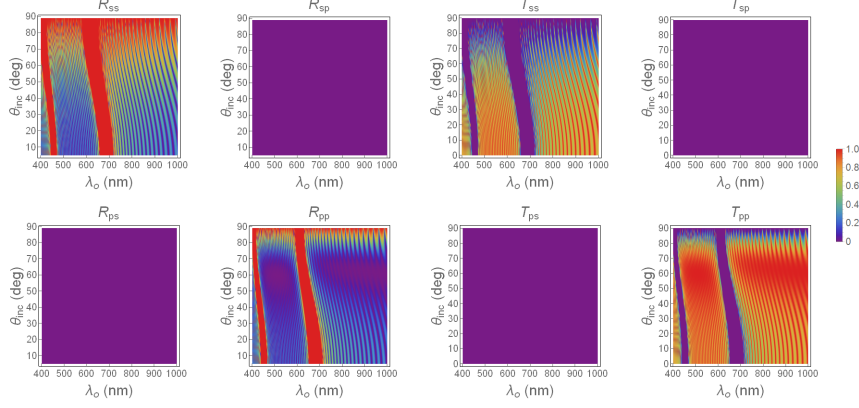


Figure 3: Density plots of all four reflectances and all four transmittances calculated as functions of  $\lambda_0$  and  $\theta_{\text{inc}}$  for a Bragg mirror comprising  $\text{TiO}_2$  CTFs with  $\chi_{v_1} = 20^\circ$ ,  $\chi_{v_2} = 70^\circ$ ,  $L_1 = 77.5$  nm, and  $L_2 = 232.5$  nm (similar to Sample A), when  $\psi = 0^\circ$ . All calculations were made with  $N = 30$ .

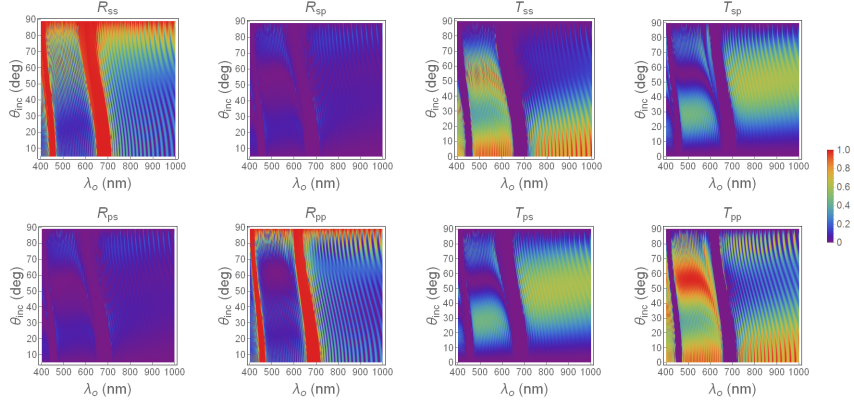


Figure 4: Same as Fig. 3, except that  $\psi = 90^\circ$ .

### 3.2.2 Chevronic STF

Next, let us present the spectrums of all eight remittances calculated for a ChevSTF comprising  $\text{TiO}_2$  CTFs with  $\chi_{v_1} = \chi_{v_2} = 20^\circ$  and  $L_1 = L_2 = 155$  nm (similar to Sample B). Figure 5 presents these remittances as functions of  $\lambda_0 \in [400, 1000]$  nm and  $\theta_{\text{inc}} \in [0^\circ, 90^\circ]$  when  $\psi = 0^\circ$ . Although  $\lambda_{0_{p_2}}^{Br} = 550.41$  nm and  $\lambda_{0_{p_2}}^{Br} = 540.32$  nm when  $\theta_{\text{inc}} = \psi = 0^\circ$ , according to Eqs. (19) and (20), no evidence of the Bragg phenomenon of order  $m = 2$  exists in Fig. 5. Furthermore, although  $\lambda_{0_{s_1}}^{Br} = 1100.82$  nm,  $\lambda_{0_{p_1}}^{Br} = 1080.64$  nm,  $\lambda_{0_{s_3}}^{Br} = 366.94$  nm, and  $\lambda_{0_{p_3}}^{Br} = 360.21$  nm are predicted by Eqs. (19) and (20) for  $\theta_{\text{inc}} = \psi = 0^\circ$ , we have verified by direct calculation that the Bragg phenomenon of order  $m \in \{1, 3\}$  is also not manifested for the chosen chevronic STF. This is evident from the plot of  $R_{pp}$  in Fig. 6 for  $\lambda_0 \in [400, 1200]$  nm and  $\theta_{\text{inc}} \in [0^\circ, 90^\circ]$ .

For  $\psi = 90^\circ$ , the situation changes somewhat. In Fig. 7, the Bragg phenomenon of order  $m = 2$  is present in the plots of  $R_{ss}$ ,  $R_{pp}$ ,  $T_{ss}$ , and  $T_{pp}$ . But this existence is vestigial at best, as it is evident in very narrow spectral regimes and that too only for  $\theta_{\text{inc}} \gtrsim 40^\circ$ . The same characteristic holds true for the Bragg phenomenon of order  $m \in \{3, 4, 5\}$ , as exemplified by Fig. 8.

The situation is somewhat different for the Bragg phenomenon of order  $m = 1$ . High-reflectance bands exist in the plots of  $R_{ps}$  and  $R_{ss}$  for  $\theta_{\text{inc}} \gtrsim 20^\circ$ , indicating that reflection is accompanied by a rotation of the vibration ellipse by angles close to  $\pm 85^\circ$ . In other words, the Bragg phenomenon is accompanied by

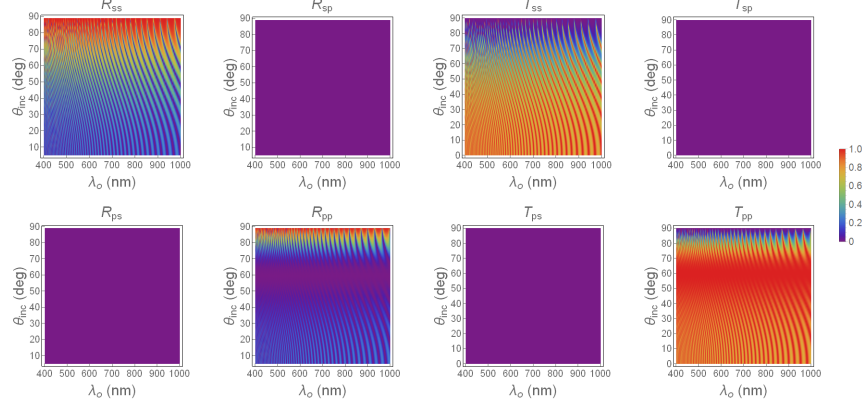


Figure 5: Density plots of all four reflectances and all four transmittances calculated as functions of  $\lambda_0$  and  $\theta_{\text{inc}}$  for a ChevSTF comprising  $\text{TiO}_2$  CTFs with  $\chi_{v_1} = \chi_{v_2} = 20^\circ$  and  $L_1 = L_2 = 155$  nm (similar to Sample B), when  $\psi = 0^\circ$ . All calculations were made with  $N = 30$ .

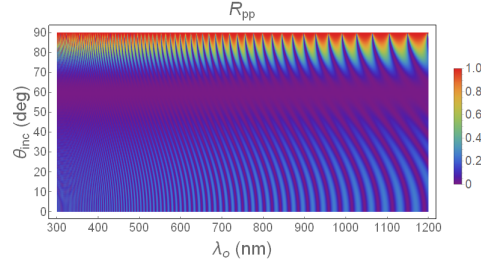


Figure 6: Density plot of  $R_{\text{pp}}$  calculated as a function of  $\lambda_0$  and  $\theta_{\text{inc}}$  for a ChevSTF comprising  $\text{TiO}_2$  CTFs with  $\chi_{v_1} = \chi_{v_2} = 20^\circ$  and  $L_1 = L_2 = 155$  nm (similar to Sample B), when  $\psi = 0^\circ$ .

significant polarization conversion, but even that is not manifested for normal and near-normal incidences.

The foregoing conclusions from examination of computed data can be explained through Eqs. (14) and (16). For normal incidence, the matrix  $[\mathbf{P}(\xi; \varepsilon_a, \varepsilon_b, \varepsilon_c)]$  simplifies to yield

$$\begin{aligned}
 [\mathbf{P}(\chi; \varepsilon_a, \varepsilon_b, \varepsilon_c)] \Big|_{\theta_{\text{inc}}=0} &= [\mathbf{P}(\pi - \chi; \varepsilon_a, \varepsilon_b, \varepsilon_c)] \Big|_{\theta_{\text{inc}}=0} \\
 &= \omega \begin{bmatrix} 0 & 0 & 0 & \mu_0 \\ 0 & 0 & -\mu_0 & 0 \\ 0 & -\varepsilon_0 \varepsilon_c & 0 & 0 \\ \varepsilon_0 \frac{\varepsilon_a \varepsilon_b}{\varepsilon_a \cos^2 \chi + \varepsilon_b \sin^2 \chi} & 0 & 0 & 0 \end{bmatrix}. \tag{23}
 \end{aligned}$$

Then, both CTFs in the unit cell of a ChevSTF are electromagnetically identical and the structural periodicity of the ChevSTF does not translate into electromagnetic periodicity. Accordingly, the Bragg phenomenon cannot be exhibited for  $\theta_{\text{inc}} = 0^\circ$ .

As  $\theta_{\text{inc}}$  increases, first the second term and then the third and fourth terms on the right side of Eq. (14) become increasingly consequential. Therefore,  $[\mathbf{P}(\chi; \varepsilon_a, \varepsilon_b, \varepsilon_c)]$  begins to differ from  $[\mathbf{p}(\pi - \chi; \varepsilon_a, \varepsilon_b, \varepsilon_c)]$ , but

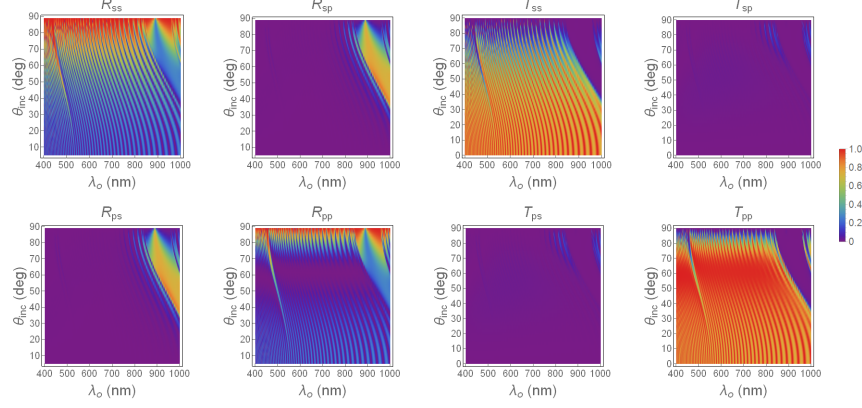


Figure 7: Same as Fig. 5, except that  $\psi = 90^\circ$ .

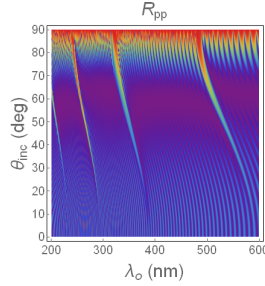


Figure 8: Same as Fig. 6, except that  $\psi = 90^\circ$ .

the difference

$$\begin{aligned}
 & [\mathbf{P}(\chi; \varepsilon_a, \varepsilon_b, \varepsilon_c)] - [\mathbf{P}(\pi - \chi; \varepsilon_a, \varepsilon_b, \varepsilon_c)] \\
 &= 2k_0 \frac{(\varepsilon_a - \varepsilon_b) \sin \theta_{\text{inc}}}{\varepsilon_a \cos^2 \chi + \varepsilon_b \sin^2 \chi} \sin \chi \cos \chi \begin{bmatrix} \cos \psi & 0 & 0 & 0 \\ \sin \psi & 0 & 0 & 0 \\ 0 & 0 & 0 & 0 \\ 0 & 0 & -\sin \psi & \cos \psi \end{bmatrix} \quad (24)
 \end{aligned}$$

stems only from the second term on the right side of Eq. (14). Hence, the Bragg phenomenon would very weakly exhibited for near-normal incidence. For more appreciable exhibition,  $\theta_{\text{inc}}$  would have to exceed some threshold value that depends not only on the values of  $\varepsilon_{a,b,c}$  and  $\chi$  but also of  $\psi$ . Equation (14) also indicates that polarization conversion is not possible when  $\sin \psi = 0$  [15].

### 3.3 Experimental Results

#### 3.3.1 Bragg mirror

Following Sec. 3.2, let us begin with the measured spectrums of all eight remittances of Sample A, which is expected to perform as a Bragg mirror. Figure 9 presents the reflectances as functions of  $\theta_{\text{inc}} \in [10^\circ, 70^\circ]$  and transmittances as functions of  $\theta_{\text{inc}} \in [0^\circ, 70^\circ]$  for  $\lambda_o \in [500, 900]$  nm when  $\psi = 0^\circ$ . As predicted in Sec. 3.2, the Bragg phenomenon of order  $m = 2$  is evident as a high-reflectance band each in the plots of  $R_{\text{ss}}$  and  $R_{\text{pp}}$  and as a low-transmittance band each in the plots of  $T_{\text{ss}}$  and  $T_{\text{pp}}$ . Let us note  $R_{\text{ss}}$  exceeds  $R_{\text{pp}}$  in the high-reflectance band, especially as  $\theta_{\text{inc}}$  increases. The center wavelengths  $\lambda_{0_{\text{ss}2}}^{\text{Br}}$  and  $\lambda_{0_{\text{pp}2}}^{\text{Br}}$  for  $\theta_{\text{inc}} = 0^\circ$  nearly overlap at approximately 700 nm and 695 nm, respectively, in the plots of  $T_{\text{ss}}$  and  $T_{\text{pp}}$ . The Bragg phenomenon of order  $m \neq 2$  lies outside the spectral range of our apparatus.

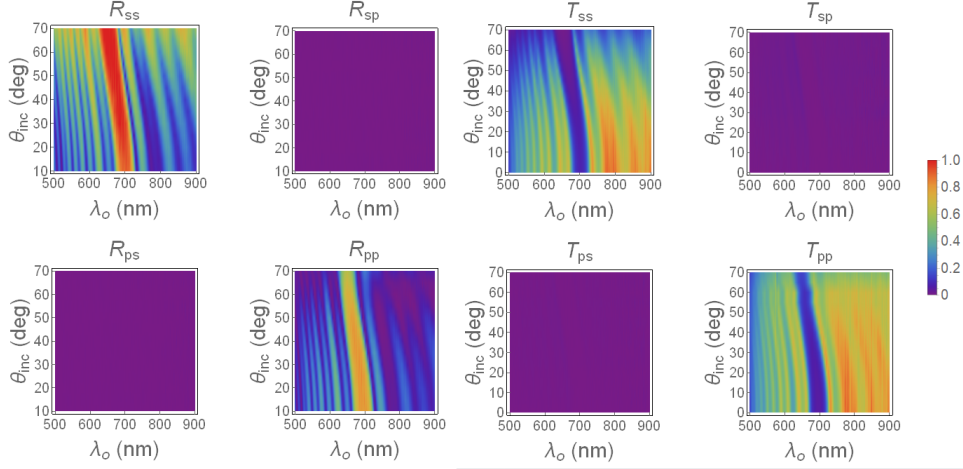


Figure 9: Density plots of all four reflectances and all four transmittances measured as functions of  $\lambda_0$  and  $\theta_{\text{inc}}$  for Sample A (see Fig. 1) when  $\psi = 0^\circ$ .

Figure 10 presents the measured remittances of Sample A when  $\psi = 90^\circ$ . Again, the Bragg phenomenon of order  $m = 2$  is evident in the plots of  $R_{\text{ss}}$ ,  $R_{\text{pp}}$ ,  $T_{\text{ss}}$ , and  $T_{\text{pp}}$ . The center wavelengths are  $\lambda_{0_{s_2}}^{\text{Br}} = 710$  nm and  $\lambda_{0_{p_2}}^{\text{Br}} = 720$  nm for  $\theta_{\text{inc}} = 10^\circ$  are somewhat redshifted with respect to those for  $\psi = 0^\circ$  in Fig. 9, in contrast to the slight blueshifts suggested by the theoretical results presented in Figs. 3 and 4.

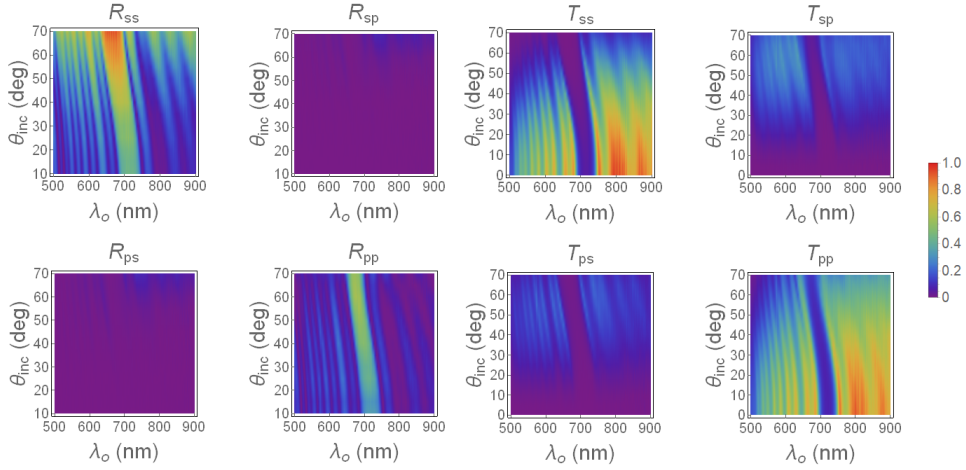


Figure 10: Same as Fig. 9, except that  $\psi = 90^\circ$ .

### 3.3.2 Chevronic STF

Finally, we present the spectrums of all eight remittances measured for Sample B, which is a ChevSTF. Figure 11 presents these remittances as functions of  $\lambda_0 \in [500, 900]$  nm and  $\theta_{\text{inc}} \leq 70^\circ$  when  $\psi = 0^\circ$ , and Fig. 12 for  $\psi = 90^\circ$ . Consistently with the theoretical predictions illustrated in Figs. 5 and 6, no evidence of the Bragg phenomenon exists for  $\psi = 0^\circ$  in Fig. 9. Even the vestigial Bragg phenomenon of order  $m = 2$  predicted in Figs. 7 and 8 for highly oblique incidence and  $\psi = 90^\circ$  is absent in Fig. 12. We could not measure the remittances for  $\theta_{\text{inc}} > 70^\circ$  in order to experimentally investigate the vestigial Bragg phenomenon of order  $m = 1$ , due to the limitations of our apparatus.

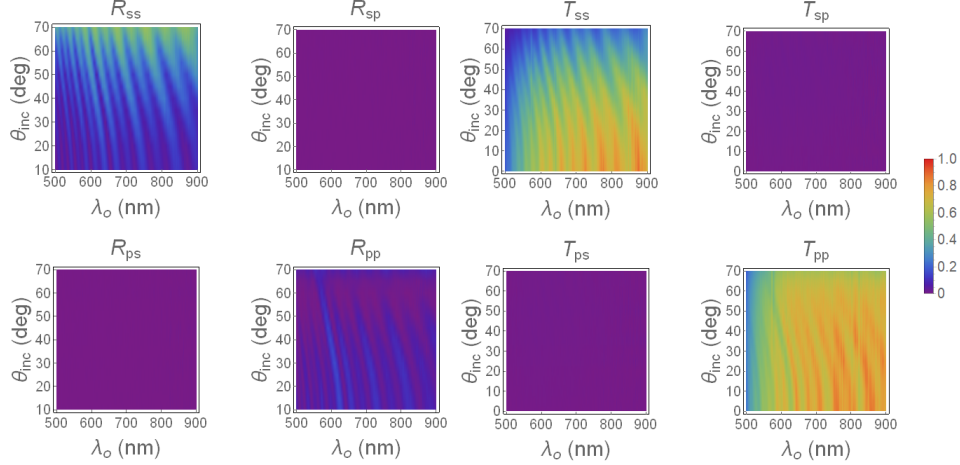


Figure 11: Density plots of all four reflectances and all four transmittances measured as functions of  $\lambda_0$  and  $\theta_{\text{inc}}$  for Sample B (see Fig. 2) when  $\psi = 0^\circ$ .

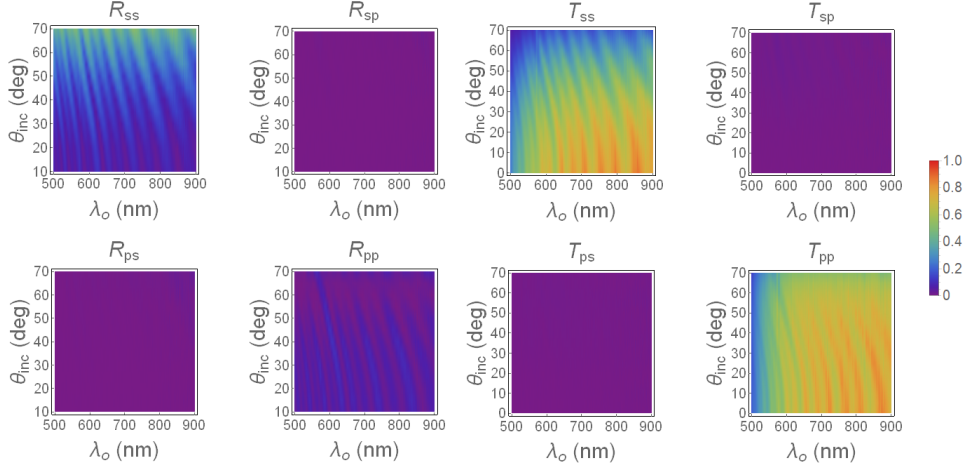


Figure 12: Same as Fig. 11, except that  $\psi = 90^\circ$ .

## 4 Concluding Remarks

The unit cell of a chevronic sculptured thin film comprises two identical columnar thin films (CTFs) except that the nanocolumns of the first are oriented at an angle  $\chi$  and nanocolumns of the second are oriented at an angle  $\pi - \chi$  with respect to the interface of the two CTFs. A CTF can be modeled as a homogeneous biaxial dielectric material for optical purposes [8]. Thus, a ChevSTF is a structurally periodic piecewise nonhomogeneous material.

Despite its structural periodicity, we determined that a ChevSTF does not exhibit the Bragg phenomenon when the wave vector of the incident plane wave lies wholly in the plane formed by the axes of the nanocolumns of the two CTFs (i.e., when  $\psi = 0^\circ$ ). This conclusion was established both theoretically and experimentally, regardless of the polarization state of the incident plane wave.

Theory indicated a vestigial manifestation of the Bragg phenomenon for highly oblique incidence when the wave vector of the incident plane wave is oriented at an angle  $\psi \in (0^\circ, 180^\circ)$  with respect to the plane formed by the axes of the nanocolumns of the two CTFs. Over the limited ranges of the free-space wavelength and the angle of incidence  $\theta_{\text{inc}}$  of our apparatus, we did not observe even that vestigial manifes-

tation. Thus, we conclude that the Bragg phenomenon would not be observed if structural periodicity does not lead to appreciable electromagnetic periodicity.

**Acknowledgments.** PDM and AL are grateful to the Charles Godfrey Binder Endowment at the Pennsylvania State University for partial financial support for this research.

## References

- [1] W. H. Bragg and W. L. Bragg, “The reflexion of X-rays by crystals,” *Proceedings of the Royal Society of London A* **88**(605), 428–438 (1913).
- [2] W. H. Bragg, “The intensity of reflexion of X rays by crystals,” *Philosophical Magazine (Series 6)* **27**(161), 881–899 (1914).
- [3] P. P. Ewald, “Zur Begründung der Kristalloptik. Teil II: Theorie der Reflexion und Brechung,” *Annalen der Physik* **49**(2), 117–143 (1916).
- [4] K. Ohtaka, “Energy band of photons and low-energy photon diffraction,” *Physical Review B* **19**(10), 5057–5067 (1979).
- [5] E. Yablonovitch, T. J. Gmitter, and K. M. Leung, “Photonic band structure: the face-centered-cubic case employing nonspherical atoms,” *Physical Review Letters* **67**(17), 2295–2298 (1991).
- [6] M. Maldovan and E. L. Thomas, *Periodic Materials and Interference Lithography*, Wiley–VCH, Weinheim, Germany (2009).
- [7] Lord Rayleigh, “On the remarkable phenomenon of crystalline reflexion described by Prof. Stokes,” *Philosophical Magazine (Series 5)* **26**(160), 256–265 (1888).
- [8] I. J. Hodgkinson and Q. h. Wu, *Birefringent Thin Films and Polarizing Elements*, World Scientific, Singapore (1997).
- [9] H. A. Macleod, *Thin-Film Optical Filters, 2nd ed.*, Institute of Physics, Bristol, United Kingdom (2001).
- [10] D.M. Mattox, *The Foundations of Vacuum Coating Technology*, Noyes Publications, Norwich, NY, USA, 2003.
- [11] P. W. Baumeister, *Optical Coating Technology*, SPIE Press, Bellingham, WA, USA (2004).
- [12] I. Hodgkinson and Q. H. Wu, “Birefringent thin-film polarizers for use at normal incidence and with planar technologies,” *Applied Physics Letters* **74**(13), 1794–1796 (1999).
- [13] H. C. Chen, *Theory of Electromagnetic Waves*, McGraw–Hill, New York, NY, USA (1983).
- [14] C. D. Gribble and A. J. Hall, *Optical Mineralogy, Principles and Practice*, University College London Press, London, United Kingdom (1992).
- [15] A. Lakhtakia and R. Messier, *Sculptured Thin Films: Nanoengineered Morphology and Optics*, SPIE Press, Bellingham, WA, USA (2005).
- [16] G. Y. Slepyan and A. S. Maksimenko, “Motohiro-Taga interface in sculptured thin films—absence of Bragg phenomena,” *Optical Engineering* **37**(10), 2843–2847 (1998).
- [17] A. Lakhtakia and R. Messier, “Reflection at the Motohiro-Taga interface of two anisotropic materials with columnar microstructures,” *Optical Engineering* **33**(8), 2529–2534 (1994).

- [18] M. Faryad and A. Lakhtakia, “The circular Bragg phenomenon,” *Advances in Optics and Photonics* **6**(2), 225–292 (2014).
- [19] S. E. Swiontek and A. Lakhtakia, “Vacuum-metal-deposition and columnar-thin-film techniques implemented in the same apparatus,” *Materials Letters* **142**(1), 291–293 (2015).
- [20] [[https://www.thorlabs.com/NewGroupPage9.cfm?ObjectGroup\\_ID=3981](https://www.thorlabs.com/NewGroupPage9.cfm?ObjectGroup_ID=3981)] (February 22, 2017).
- [21] [[http://www.tydexoptics.com/materials1/for\\_transmission\\_optics/cvd\\_znse/](http://www.tydexoptics.com/materials1/for_transmission_optics/cvd_znse/)] (accessed February 22, 2017).
- [22] [<https://www.alfa.com/en/catalog/013241/>] (accessed February 22, 2017).
- [23] I. J. Hodgkinson, Q. h. Wu, and J. Hazel, “Empirical equations for the principal refractive indices and column angle of obliquely deposited films of tantalum oxide, titanium oxide, and zirconium oxide,” *Applied Optics* **37**(13), 2653–2659 (1998).
- [24] S. Erten, A. Lakhtakia, and G. D. Barber, “Experimental investigation of circular Bragg phenomenon for oblique incidence,” *Journal of the Optical Society of America A* **32**(5), 764–770 (2015).
- [25] N. J. Severs, “Freeze-fracture electron microscopy,” *Nature Protocols* **2**(3), 547–576 (2007).
- [26] R. Messier, T. Gehrke, C. Frankel, V. C. Venogopal, W. Otaño, and A. Lakhtakia, “Engineered sculptured nematic thin films,” *Journal of Vacuum Science and Technology A* **15**(4), 2148–2152 (1997).
- [27] D. T. F. Marple, “Refractive index of ZnSe, ZnTe, and CdTe,” *Journal of Applied Physics* **35**(3), 539–542 (1964).
- [28] J. R. Devore, “Refractive indices of rutile and sphalerite,” *Journal of the Optical Society of America* **41**(6), 416–419 (1951).
- [29] W. D. St. John, W. J. Fritz, Z. J. Lu, and D.-K. Yang, “Bragg reflection from cholesteric liquid crystals,” *Physical Review E* **51**, 1191–1198 (1995).